Interstitial Defect Modulation Promotes Thermoelectric Properties of *p*-Type HfNiSn

Xin Ai, Wenhua Xue, Lars Giebeler, Nicolás Pérez, Binghua Lei, Yue Zhang, Qihao Zhang, Kornelius Nielsch, Yumei Wang,* and Ran He*

The *n*-type MNiSn (M = Ti, Zr, or Hf) half-Heusler compounds are reported as promising medium- and high-temperature thermoelectric materials; however, their *p*-type counterparts have suffered from poor performance due to the in-gap state caused by Ni occupying the tetrahedral interstitials. Inspired by recent findings that thermoelectric performance can be enhanced without substantially increasing compositional or structural complexity, the study attempts to manipulate the Ni interstitial defects by altering the stoichiometric composition. The results show that when HfNiSn is prepared by a non-equilibrium method, the intrinsic Ni defects are effectively suppressed by simply reducing the nominal Ni content. The suppression of Ni defects not only leads to a larger bandgap, but also attenuates carrier scattering to achieve higher mobility. After further optimization of the carrier concentration, the *p*-type HfNi$_{0.85}$Co$_{0.05}$Sn achieves a maximum power factor of 3100 μW m^{-1} K^{-2} at 773 K and a peak *zT* of $\approx$0.7 at 973 K, both of which are superior to that of the state-of-the-art *p*-type MNiSn. The results demonstrate that the off-stoichiometric ratio is effective in decoupling electron-phonon transports of thermoelectric materials with massive intrinsic defects, and also contribute to understanding the role of defect modulation in optimizing thermoelectric properties.

1. Introduction

Thermoelectric (TE) technology utilising waste heat to generate electricity is recognised as one of the most promising approaches to alleviate the global fossil fuel shortage and promoting ecological sustainability.[1–3] The conversion efficiency of a TE device is strongly related to the performance of TE materials, which is determined by the dimensionless figure-of-merit (*zT*). $zT = \alpha^2 \sigma T/\kappa$, where α is the Seebeck coefficient and σ the electrical conductivity, *T* is the absolute temperature, and κ is the total thermal conductivity that consists of the electronic (κ_e), lattice (κ_l), and bipolar (κ_{bip}) thermal conductivity.[4–6] Therefore, good thermoelectric materials require high Seebeck coefficients, high electrical conductivity and low thermal conductivity. However, these parameters are strongly intertwined, thus making *zT* enhancement extremely complicated.[7,8] Over the

X. Ai, L. Giebeler, N. Pérez, K. Nielsch, R. He
Leibniz Institute for Solid State and Materials Research Dresden e.V. (IFW-Dresden)
01069 Dresden, Germany
E-mail: r.he@ifw-dresden.de
X. Ai, K. Nielsch
Institute of Materials Science
TUD Dresden University of Technology
01062 Dresden, Germany
W. Xue, Y. Zhang, Y. Wang
Institute of Physics
Chinese Academy of Sciences
Beijing 100190, China
E-mail: wangym@iphy.ac.cn

B. Lei
College of Semiconductors (College of Integrated Circuits)
Condensed Matter Group
Hunan University
Changsha 410082, China
Q. Zhang
Light Technology Institute
Karlsruhe Institute of Technology
76131 Karlsruhe, Germany
K. Nielsch
Institute of Applied Physics
TUD Dresden University of Technology
01062 Dresden, Germany
Y. Wang
Beijing Branch of Songshan Lake Materials Laboratory
Dongguan, Guangdong 523808, China

past decades, a number of approaches have been devised to improve the thermoelectric properties, including carrier concentration optimization,[9] band structure engineering,[10–12] hierarchical microstructure manipulation[13–16] and entropy engineering.[17,18] Most of these strategies aim at increasing the disorder of the material and thus effectively decoupling electron and phonon transport.

In contrast, recent work has shown that reducing the defect concentration can also decouple the transport of electrons and phonons, especially for those with massive intrinsic defects.[19–21] In this regard, the TE properties of compounds can be enhanced by manipulating defects with less-alloyed compositions or even without introducing any foreign elements, different from traditional extrinsic alloying. For example, trace amounts of copper atoms are used to suppress intrinsic defects in Sn vacancies in SnSe, thereby attenuating carrier scattering from defects and increasing carrier mobility.[21] In addition, in GeTe compounds, a "compositional plainification" strategy is proposed, whereby the hole concentration is simply tuned by annealing without anti-doping or heterogeneous alloying. As a result, the carrier mobility was greatly improved due to the suppression of intrinsic vacancies.[22] Another study found that the addition of excessive Ge in GeTe compounds resulted in the same effect.[23] These strategies refer to controlling intrinsic defects in materials without involving compositional or structural complexity and present a simple yet effective approach to TE optimization. Apart from this, intrinsic defect modulation may restore the crystal structure to an ordered state, which is essential for analyzing the inherent effects of different types of defects on TE transports.

Among the various thermoelectric materials, half-Heusler (HH) compounds are one of the most promising candidates for mid- to high-temperature generators because of their high thermoelectric performance as well as their environmentally friendly, outstanding thermal stability and mechanical robustness.[24,25] Among them, n-type MNiSn (M = Ti, Zr, Hf) stands out with zT exceeding 1.0 through strategies such as aliovalent doping, isoelectronic alloying, and nanostructuring.[26–29] In contrast, the thermoelectric properties of p-type MNiSn are still much lower than their n-type counterparts, which limits the development of MNiSn-based thermoelectric devices. The experimental results contradict first-principle calculations, which predicted that the TE properties of p-type MNiSn could be similar to those of n-type compounds.[30] However, the current experimental results are far from expectations. Recent findings suggest that this disparity originates from the formation of interstitial Ni defects, that is, certain Ni atoms occupying otherwise vacant 4d (3/4, 3/4, 3/4) lattice sites in nominally stoichiometric polycrystalline MNiSn.[31,32] On one hand, these interstitial Ni defects can be ionized to provide electrons, which gives rise to an overall n-type conductive characteristic in the absence of any chemical doping.[33] On the other hand, an "impurity band" is induced in the forbidden band, resulting in a narrowing of the bandgap (E_g) to 0.15 eV.[31–33] As a result, a bipolar effect occurs at lower temperatures, thereby severely deteriorating the zT of p-type MNiSn compounds. Therefore, to achieve high-performance p-type MNiSn, it is desirable to first suppress the interstitial Ni defects to realize a primitive defect-free structure without introducing compositional or structural complexity.

The large difference in electronegativity between Ni and Hf atoms in HfNiSn is favourable for the stabilization of Ni atoms and the suppression of intrinsic interstitial Ni defects.[34,35] In this regard, we synthesize HfNi$_{1-x}$Sn compounds with nominal Ni deficiency. To avoid the formation of interstitial Ni defects due to rapid crystal growth during high-temperature melting, we employ a non-equilibrium approach that combines mechanical alloying and spark plasma sintering. As a result, the off-stoichiometric composition of HfNi$_{1-x}$Sn is largely tunable over a range of x (up to 0.1 in this work) without secondary-phase formation based on energy dispersive X-ray (EDS) analysis. The Ni deficiency eliminates the in-gap state and gives rise to the "real" bandgap (E_g) of HfNiSn (**Figure 1a**). The bandgap obtained from the resistivity measurement (E_{g_re}) of HfNi$_{1-x}$Sn ($x = 0.1$) is ≈0.4 eV, which is higher than that of previously reported MNiSn polycrystals[36] and close to that of ZrNiSn single crystals[37] (Figure 1b). Further doping with cobalt adjusts the carrier concentration. The optimized composition, HfNi$_{0.85}$Co$_{0.05}$Sn, maintains a Goldsmid-Sharp bandgap[38] (E_{g_GS}) of 0.33 eV, still higher than the literature values of MNiSn[32,35,39] (Figure 1c). Moreover, by suppressing as many intrinsic Ni defects as possible, carrier scattering is attenuated, leading to an increase in carrier mobility (Figure 1a). The weighted mobility (μ_W) is thus elevated to 285 cm^{-2}V^{-1}s^{-1} along with an exceptional power factor($\alpha^2\sigma$) of 2300 μWm^{-1}K^{-2} at room temperature, outperforming the reported state-of-the-art p-type MNiSn compounds[32,35,40,41] (Figure 1d). Finally, in combination with the reduced lattice thermal conductivity, a zT of ≈0.7 is achieved in HfNi$_{0.85}$Co$_{0.05}$Sn at 973 K, which is the highest value among existing p-type MNiSn.

2. Results and Discussion

We first calculated the electronic band structures of HfNiSn compounds with different defect concentrations and investigated the contribution of suppressed Ni interstitial defects to the bandgap. It is found when the interstitial Ni concentration decreases from 9.4% (three Ni 4d atoms in $2 \times 2 \times 2$ supercell) to 3.1% (one Ni 4d atom in $2 \times 2 \times 2$ supercell), the dispersion of the impurity bands narrows, yielding a bandgap widening of HfNiSn (**Figure 2a**,b). If the Ni interstitial defects can be completely suppressed, a "true" bandgap of 0.4 eV is exposed (Figure 2c). Besides, further calculation results suggested that the Ni deficit at the 4c position which is an order site for Ni as shown in Figure S1a (Supporting Information), has no significant effect on the energy band structure, regardless of whether Ni is present at the 4d site or not (Figure S1b,c, Supporting Information).

In light of this, we synthesized HfNi$_{1-x}$Sn ($x = 0, 0.05, 0.1$, and 0.15) by a facile process combining mechanical alloying and spark plasma sintering. XRD measurements on bulk samples indicate that all HfNi$_{1-x}$Sn are successfully synthesized with the same half-Heusler phase (Figure S2, Supporting Information). All XRD patterns are well indexed with a cubic MgAgAs-type crystal structure with the space group F-43m.[24,42] The actual sample compositions determined by the inductively coupled plasma optical emission spectroscopy (ICP-OES) closely match their nominal compositions (Table S1, Supporting Information). In addition, some signals of impurity phases with very low intensity compared to the main half-Heusler phase are detected in the XRD patterns of all samples. However, the backscattered
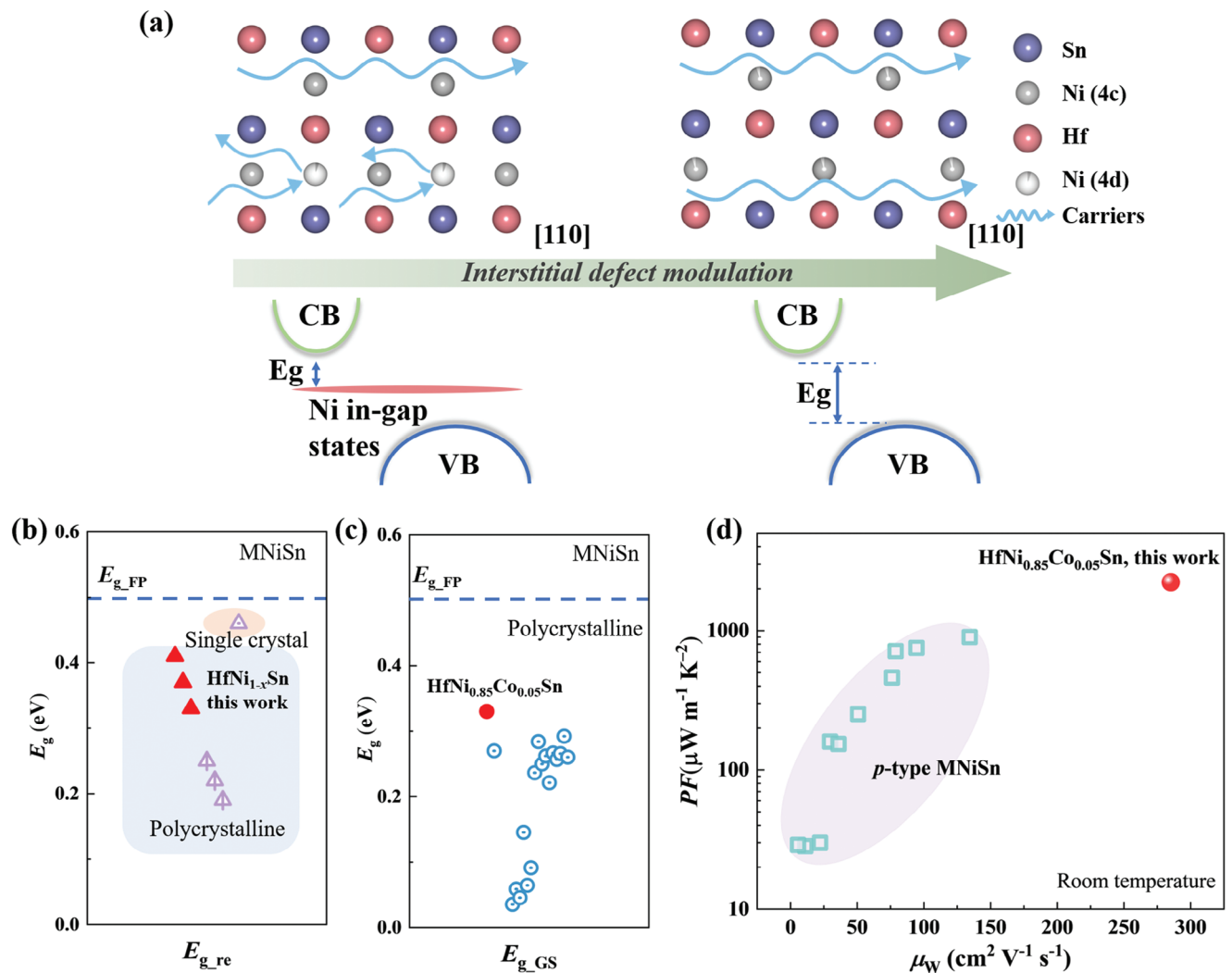
**ADVANCED
SCIENCE NEWS**

www.advancedsciencenews.com

**ADVANCED
ENERGY
MATERIALS**

www.advenergymat.de

Figure 1. Bandgap enlargement and optimization of electrical properties by interstitial defect modulation in HfNiSn. a) Schematic showing the strategy to suppress the intrinsic defects of HfNiSn, thereby increasing the bandgap and weakening carrier scattering. b) Energy bandgap E_{g_re} of MNiSn obtained from resistivity measurements.[35–37] c) Goldsmid-Sharp bandgap E_{g_GS} of MNiSn.[32,35,39] d) Comparison of power factor and weighted mobility at room temperature of Hf(Ni,Co)$_{0.9}$Sn in this study with the reported state-of-the-art p-type MNiSn.[32,35,40,41]

electron images and corresponding elemental mappings show the presence of a Ni-deficient phase in the $x = 0.15$ sample (Figure S3, Supporting Information). We further doped HfNi$_{0.9}$Sn with cobalt (Co) to modulate the carrier concentration. The XRD patterns of bulk HfNi$_{0.9-y}$Co$_y$Sn with $0.01 \leq y \leq 0.09$ are presented in Figure S4 (Supporting Information), where all peaks are well indexed to the cubic half-Heusler phase. The uniform distributions of Hf, Ni, Sn, and Co are confirmed by elemental mappings in Figure S5 (Supporting Information).

Subsequently, the amount of Ni interstitial defects in the HfNi$_{0.95}$Sn, HfNi$_{0.9}$Sn, HfNi$_{0.85}$Sn and HfNi$_{0.85}$Co$_{0.05}$Sn compounds is estimated through powder XRD patterns using the Rietveld method[43] (Figure 2d,e; Figure S6, Supporting Information). The first step is to perform phase analyses, which shows that as the Ni content decreases, the number of phases other than HfNiSn increases, such as Hf and Hf-Sn alloy or HfO$_2$ which may be a residue of the metal before synthesis or a reaction prod-

uct of the metal with traces of residual oxygen during the syntheses processes. This result implies that some Hf and Sn are lost during the formation of the main half-Heusler phase, thus the actual compositions remain consistent with the stoichiometric ratio of HfNiSn. After the exclusion of impurity phases, structural models with different refinement scenarios, such as refinements with or without 4c and 4d coupling as well as mixed occupancies of certain crystalline sites, are used to achieve a variety of occupancy capacities and to arrive at the most probable results. As a result, by careful refining the 4d position occupancy, the Ni 4d interstitial defects in the Ni-deficient samples are <1%, which is lower than that of pristine HfNiSn[35] (3.3%, Figure 2f). The 4d occupancy slightly increases with higher Ni deficiency, probably due to the lack of Ni leading to a p-type growth, which triggers n-type self-compensating defects (i.e., Ni 4d interstitials in this case).[33,44] Specifically, the amounts of 4d interstitial Ni defects in HfNi$_{0.9}$Sn and HfNi$_{0.85}$Co$_{0.05}$Sn are estimated to ≈0.5%. These
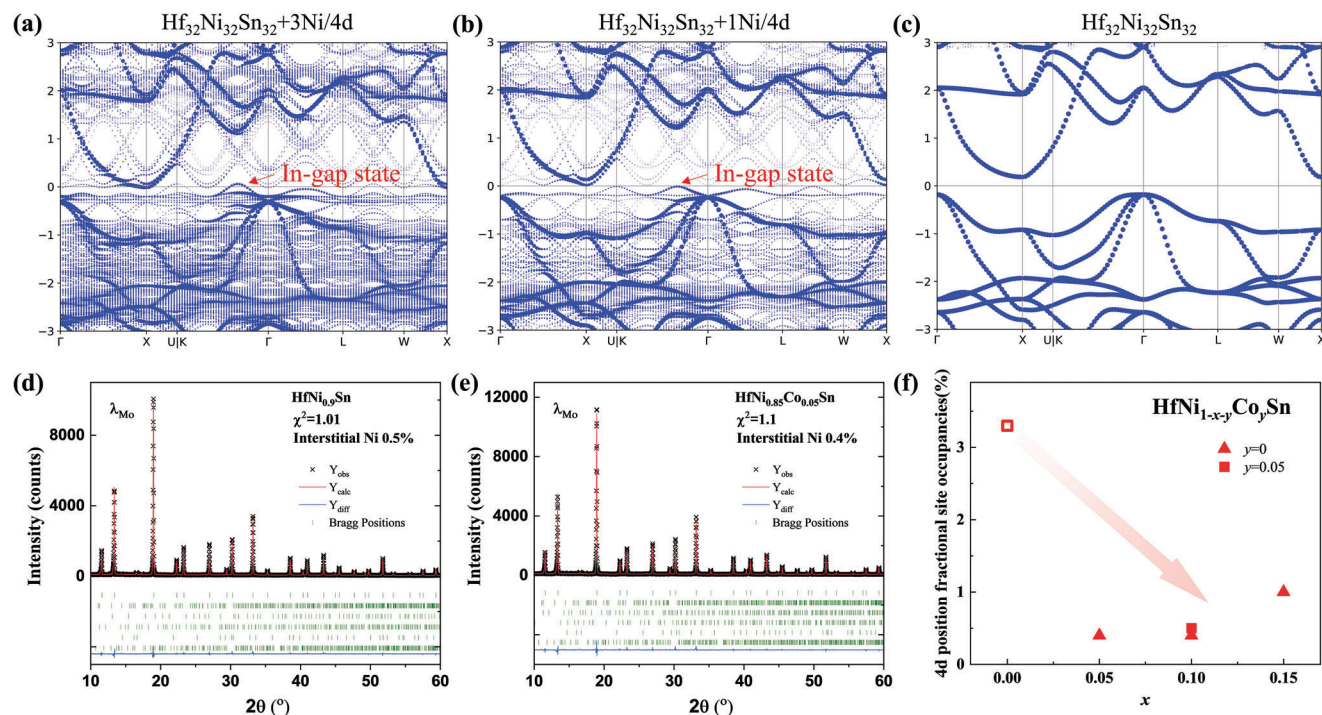
Figure 2. Influence of insufficient Ni on formation of Ni 4d interstitial defects and band structure. Calculated band structure of a) $Hf_{32}Ni_{32}Sn_{32}$ with three Ni 4d interstitial defects, b) $Hf_{32}Ni_{32}Sn_{32}$ with one Ni 4d interstitial defect, and c) $Hf_{32}Ni_{32}Sn_{32}$ without Ni 4d interstitial defects. d) X-ray powder diffraction pattern of $HfNi_{0.9}Sn$ together with Rietveld refinement result. Bragg markers corresponding to the half-Heusler phase are used to fit the pattern. The markers from top to bottom are assigned to HfNiSn, HfO_2, Ni_3Sn, Hf_5Sn_3, Hf and Ni_3Sn_4, respectively. e) X-ray powder diffraction pattern of $HfNi_{0.85}Co_{0.05}Sn$ and its Rietveld refinement result. The markers from top to bottom are assigned to Hf(Ni,Co)Sn, HfO_2, Hf_5Sn_3, $HfSn_2$, Hf and Ni_3Sn_4, respectively. f) Comparison of Ni 4d occupancies of different $HfNi_{1-x-y}Co_ySn$ samples. The value of pristine HfNiSn is taken from reference.[35]

miniature values indicate that the deficiency of Ni is effective in inhibiting the formation of interstitial defects.

To further evaluate the occupancies of the Ni sites located at the Wyckoff position 4c and 4d from a microstructural perspective, transmission electron microscopy (TEM) and Cs-corrected high-angle annular dark field scanning transmission electron microscopy (HAADF-STEM) investigations were performed on HfNiSn, $HfNi_{0.9}Sn$ and $HfNi_{0.85}Co_{0.05}Sn$. The selected area electron diffraction patterns (Figure S7, Supporting Information) for all three samples can been successfully indexed according to the structure of F-43m space group. HAADF-STEM images provide direct projections at the atomic level with a contrast roughly proportional to $Z^{1.7}$, where Z is the atomic number.[45] **Figure 3a–c** shows the HAADF-STEM images of HfNiSn, $HfNi_{0.9}Sn$, and $HfNi_{0.85}Co_{0.05}Sn$, respectively, which are taken along the [110] direction to avoid the overlap of different Wyckoff positions. The intensity profiles in Figure 3d,g,j obtained from the cyan dashed boxes of Figure 3a–c shows strong, moderate, and weak intensities corresponding to Hf ($Z = 72$), Sn ($Z = 50$), and Ni or Co atoms ($Z = 28$ and 27), respectively. According to these profiles, in the HfNiSn samples, the intensity at 4d sites is close to that at 4c sites (Figure 3d), whereas in the $HfNi_{0.9}Sn$ and $HfNi_{0.85}Co_{0.05}Sn$ samples, the difference between 4c and 4d sites is greater (Figure 3f,j). This suggests that there are fewer Ni atoms distributed at the 4d sites in Ni-deficient samples.

To better display the distribution of Ni in different samples, we counted the intensities at 4c and 4d position in the whole HAADF-STEM image. 3D normalized stereograms are presented, where the intensities at 4c and 4d sites are inversely related to each other, which signifies that the formation of interstitial Ni is not only due to excess Ni, but also probably partially attributed to Frenkel defects.[46] As shown in Figure 3e,f, the intensity at 4d sites is comparable to that at 4c sites in the HfNiSn sample, which suggests that the 4d site has a relatively high probability of occupation. In contrast, for the Ni-deficient samples, the Ni atoms tend to be concentrated at 4c sites, and the relative intensity at 4d sites is lower (Figure 3h,i,k,l). The TEM results indicate that the 4d interstitial Ni content is reduced in Ni-deficient samples compared to pristine HfNiSn, which is consistent with the results of the Rietveld analyses of the XRD patterns. Therefore, the off-stoichiometric strategy without compositional or structural complexity has an inhibitory effect on the formation of intrinsic interstitial Ni defects of HfNiSn.

The electrical transport properties of $HfNi_{1-x}Sn$ ($x = 0$, 0.05, 0.1, and 0.15) samples are shown in **Figure 4**. As presented in Figure 4a, the Seebeck coefficient at room temperature is shifted from negative to positive with increasing Ni deficiency, which indicates that the dominant carriers gradually change from electrons to holes. However, due to the bipolar diffusion caused by the inadequate concentration of hole carriers, the Seebeck coefficients of $HfNi_{0.9}Sn$ and $HfNi_{0.85}Sn$ turn negative at elevated temperatures. The electrical resistivity of $HfNi_{1-x}Sn$ shows a monotonous decrease with increasing temperature (Figure 4b), exhibiting typical semiconductor conductive

**ADVANCED
SCIENCE NEWS**

www.advancedsciencenews.com
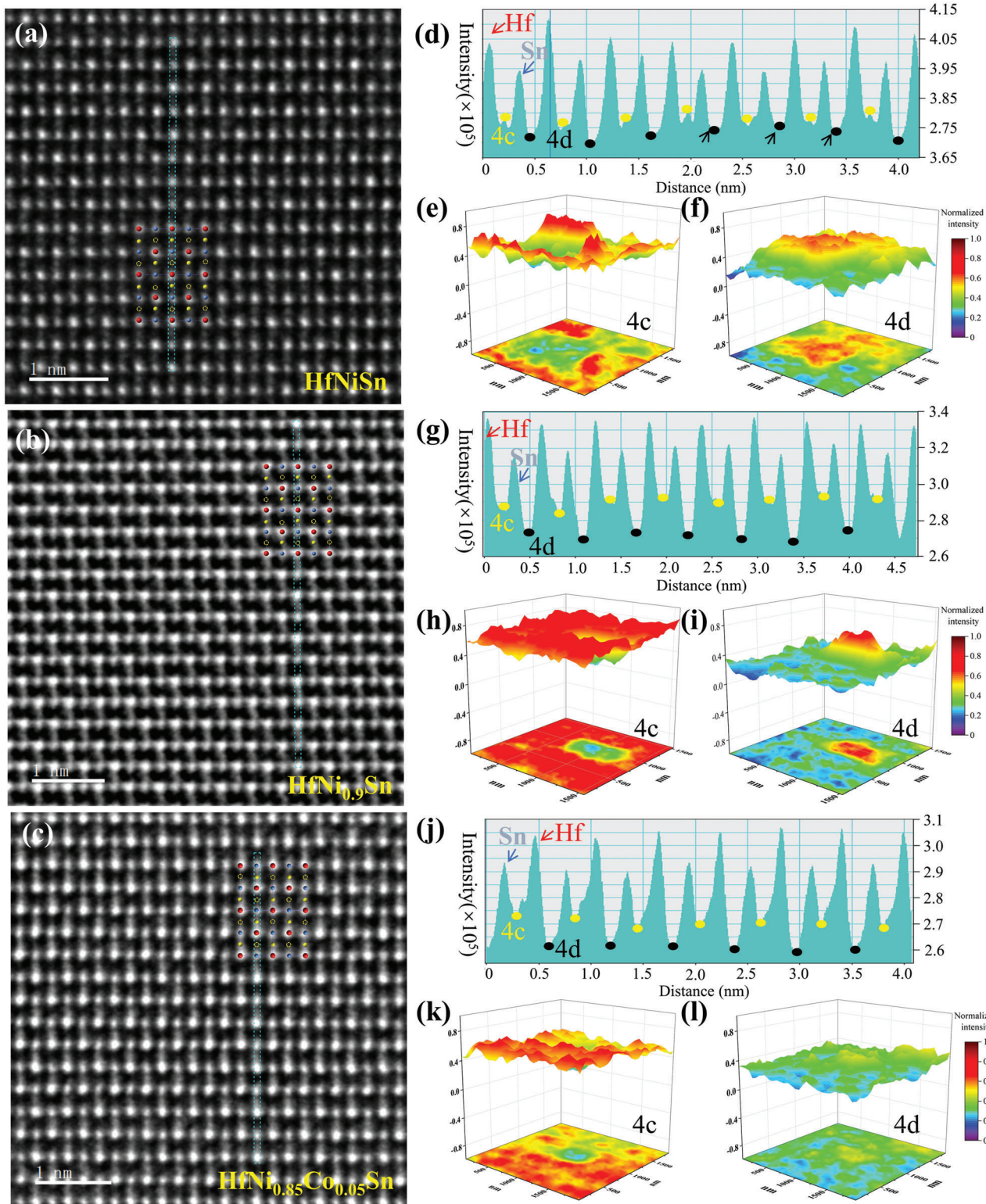
**ADVANCED
ENERGY
MATERIALS**

www.advenergymat.de

Figure 3. Comparison of 4d position occupancy in pristine HfNiSn and Ni-deficient samples. a–c) HAADF-STEM images of HfNiSn, $HfNi_{0.9}Sn$, and $HfNi_{0.85}Co_{0.05}Sn$ along the [110] direction, respectively. The red, blue, and yellow balls represent Hf, Sn, and Ni, respectively. The yellow dotted circles indicate the 4d sites. d) Intensity profile across the horizontal cyan dashed box in (a). e,f) A corresponding statistical view of normalized occupied intensity distribution at 4c and 4d sites in (a). g) Intensity profile across the horizontal cyan dashed box in (b). h,i) Corresponding statistical view of normalized occupied intensity distribution at 4c and 4d sites in (b). j) Intensity profile across the horizontal cyan dashed box in (c). k,l) Corresponding statistical view of normalized occupied intensity distribution at 4c and 4d sites in (c).
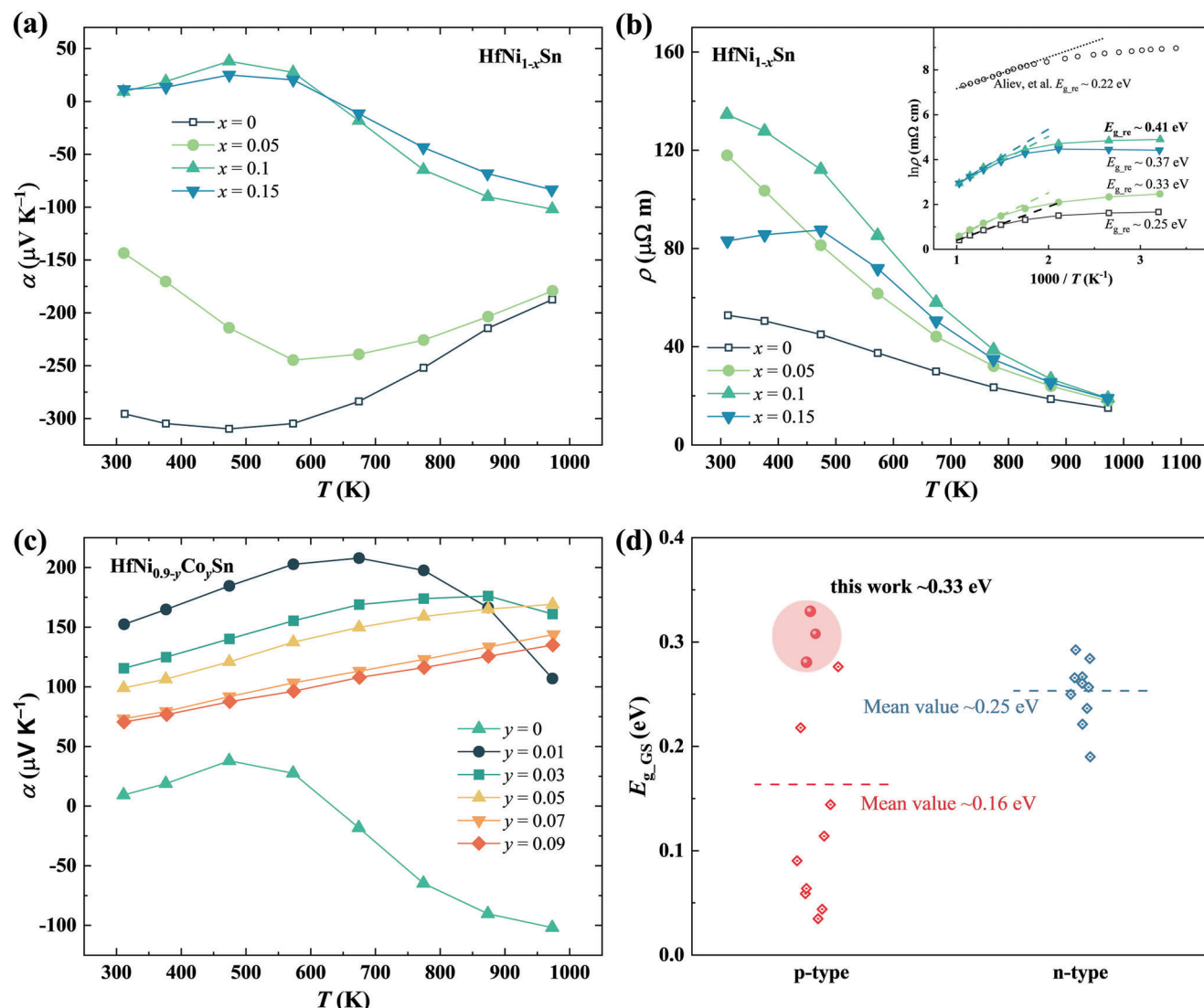
**ADVANCED
SCIENCE NEWS**

www.advancedsciencenews.com

**ADVANCED
ENERGY
MATERIALS**

www.advenergymat.de

Figure 4. Electrical transport properties of Ni-deficient samples. a) Temperature-dependent Seebeck coefficient of $HfNi_{1-x}Sn$. Data for the pristine HfNiSn sample is taken from previous work.[35] b) Temperature-dependent electrical resistivity of $HfNi_{1-x}Sn$. The inset shows the bandgap E_{g_re} that is estimated using the high-temperature resistivity data. The polycrystalline HfNiSn data for comparison is taken from Aliev et al.[36] c) Temperature-dependent Seebeck coefficient of $HfNi_{0.9-y}Co_ySn$. d) Comparison of the Goldsmid-Sharp bandgap E_{g_GS} of $HfNi_{0.9-y}Co_ySn$ with those of published MNiSn-based materials.[32,35,40,41,47]

behavior. The bandgap E_{g_re} is estimated using the high-temperature resistivity data according to the formula $\rho \approx \exp(E_{g\_re}/2k_BT)$.[37] As shown in the inset of Figure 4b, E_{g_re} of $HfNi_{0.9}Sn$ is 0.41 eV, which is nearly identical to that from the first-principles calculations in Figure 2c. Noticeably, it is nearly twice as high as the one obtained from polycrystalline HfNiSn samples in previous work[36] and close to the 0.46 eV of single-crystalline ZrNiSn.[37]

Although $HfNi_{0.9}Sn$ and $HfNi_{0.85}Sn$ samples with Ni deficiency exhibit p-type semiconductor characteristics at room temperature, their thermoelectric properties are not satisfactory owing to the low hole concentration and high thermal conductivity (Figure S8, Supporting Information). To further enhance the thermoelectric properties, we introduced Co as an aliovalent element to partially substitute Ni. As a result, Co doping effectively

increases the hole concentration (Figure S9, Supporting Information) and thereby enhances the electrical transport properties. As shown in Figure 4c, the Seebeck coefficient increases dramatically from ≈10 μV K^{-1} for $HfNi_{0.9}Sn$ to ≈150 μV K^{-1} for $HfNi_{0.89}Co_{0.01}Sn$ at room temperature, and the latter remains positive over the whole temperature range. With further increase of the Co content, the maximum α of $HfNi_{0.9-y}Co_ySn$ samples decreases gradually, but the peak moves toward higher temperatures, which suggests a more degenerate p-type semiconductor transport behavior. Further, the Goldsmid-Sharp thermopower bandgap of $HfNi_{0.9-y}Co_ySn$ is derived from the formula $E_{g\_GS} = 2eT_{max}\alpha_{max}$, where α_{max} is the maximum Seebeck coefficient and T_{max} is the absolute temperature at which α_{max} occurs.[38] As illustrated in Figure 4d, the maximum E_{g_GS} of the $HfNi_{0.9-y}Co_ySn$ samples is ≈0.33 eV, which is higher than those of the n- and

ADVANCED
SCIENCE NEWS

www.advancedsciencenews.com

**ADVANCED
ENERGY
MATERIALS**

www.advenergymat.de

p-type MNiSn samples in previous literature.[32,35,40,41,47] These results agree with the calculations that reducing interstitial Ni defects in Hf(Ni,Co)Sn can expand the bandgap. Therefore, it is concluded that altering the Ni stoichiometry ensures the availability of high-quality HfNiSn samples with fewer interstitial Ni defects leading to a desirably enlarged bandgap.

Corresponding to the change in the Seebeck coefficient, the enhancement of electrical conductivity also suggests that Co doping leads to an increase in carrier concentration (**Figure 5a**). The carrier concentration gradually increases from 5.23×10^{20} cm^{-3} to 2.48×10^{21} cm^{-3} as the Co doping reaches 9%. More critically, the electrical conductivity of HfNi$_{0.9-y}$Co$_y$Sn is much higher compared to the Hf(Ni,Co)$_1$Sn and Zr(Ni,Ir)$_{1.3}$Sn samples which have similar carrier concentrations.[35,41] It is evident from the temperature dependence of the conductivity that the correlation exponent gradually changes from 0.13 to −0.6 as the stoichiometric ratio of Ni decreases. This variation implies that insufficient Ni composition weakens the defect-induced carrier scattering[48] which is well reflected by the weighted mobility μ_w. As shown in Figure 5b, μ_w has a strong dependence on the stoichiometric ratio near room temperature and gradually increases with decreasing Ni content at similar carrier concentrations, such as Hf(Ni,Co)$_{0.9}$Sn with $\approx 1.1 \times 10^{21}$ cm^{-3} and Hf(Ni,Co)$_1$Sn with $\approx 1.04 \times 10^{21}$ cm^{-3} or Hf(Ni,Co)$_{0.9}$Sn with $\approx 1.61 \times 10^{21}$ cm^{-3} and Hf(Ni,Co)$_1$Sn with $\approx 1.5 \times 10^{21}$ cm^{-3}. The large increase in μ_w suggests that the electrical transport properties are well optimized by plainifying the elemental composition to modulate the scattering mechanism.

To elucidate the effect of Ni deficiency on the structure of the energy band, the density-of-states (DOS) effective mass m^* is estimated based on the single parabolic band (SPB) model (Supporting information) with values up to $m^* \approx 6.5$ m_e (Figure S10, Supporting Information). Therefore, large Seebeck coefficients can be obtained even at high carrier concentrations. Furthermore, this value is in accordance with our previous findings for *p*-type HfNiSn ($m^* \approx 7$ m_e), which is probably due to the fact that the valence band of MNiSn has little dependence on Ni, and thus Ni-deficiency do not cause a significant change in the effective mass of the valence band at the Γ point.[49] Assuming the same m^* for Hf(Ni,Co)$_{1-x}$Sn, the carrier-concentration dependence of the mobility is evaluated and shown in Figure 5c. It is indicated that the mobility obtained in $x \geq 0.1$ samples is doubled compared to that of $x = 0$ over the whole range of n_H, and that μ_H tends to increase at similar n_H as the amount of nickel deficiency (x) increases. This enables a higher electrical conductivity at the same Seebeck coefficient. Moreover, the doping efficiency of the element (cobalt) increases as well (Figure S11, Supporting Information). The enhanced hole doping efficiency further supports the minimized interstitial defects at the 4d sites, which are known to impair the *p*-type doping efficiency. Due to the largely enhanced Seebeck coefficient and relatively high electrical conductivity, the power factor approaches 2300 μW m^{-1} K^{-2} at room temperature and reaches a maximum value of 3100 μW m^{-1} K^{-2} at 773 K, which is much higher than the previously reported values[35] (Figure 5d).

Figure 5e shows the thermal conductivity of HfNi$_{0.9-y}$Co$_y$Sn samples. The total thermal conductivity decreases from 8.3 to 7 W m^{-1} K^{-1} at 300 K due to the suppression of lattice thermal conductivity. The decrease of lattice thermal conductivity is mainly

due to the introduction of point defects and lattice softening as reported in our previous work.[35] Clearly, Co doping has a synergetic effect on the thermoelectric properties of HfNi$_{0.9}$Sn, optimizing both the electrical and thermal transport properties. A notable zT improvement is realized with a peak value of ≈ 0.7 at 973 K in HfNi$_{0.85}$Co$_{0.05}$Sn (Figure 5f). In addition, the samples exhibit consistent performance during the repeat measurements (Figure S12, Supporting Information), indicating that the nickel defects are thermally and chemically stable. Compared to the previously reported *p*-type MNiSn compounds synthesized at stoichiometric ratios,[32,35,41] the Ni-deficient sample in this work presents the highest zT due to a larger bandgap and higher mobility.

3. Conclusion

In summary, this work demonstrates that the thermoelectric properties of *p*-type HfNiSn can be enhanced substantially by an off-stoichiometric strategy without complex composition or structure. The HfNiSn-based compounds with Ni content deviating from the stoichiometric ratio are successfully synthesised by a non-equilibrium method. The Rietveld analysis of XRD data and scanning transmission electron microscopy confirm that changing the stoichiometric ratio effectively inhibits the formation of Ni 4d interstitial defects. As a result, the HfNi$_{1-x-y}$Co$_y$Sn samples exhibit a larger bandgap and higher carrier mobility. A high zT of 0.7 at 973 K is achieved in Ni-deficient HfNi$_{0.85}$Co$_{0.05}$Sn sample, which is superior to previously reported MNiSn-based *p*-type thermoelectric materials. Our results deepen the understanding of MNiSn-based half-Heusler thermoelectrics, demonstrate the effectiveness of manipulating the intrinsic defects in half-Heusler system, and will reveal the potential for improving other thermoelectric materials.

4. Experimental Section

Synthesis: Raw elements including Hf powder (99.6%, Alfa Aesar), Ni powder (99.7%, Alfa Aesar), Sn powder (99.5%, Alfa Aesar) and Co powder (99.9%, MaTeck), were weighted according to the stoichiometry and loaded into ball milling jars with two stainless steel balls of 12.7 mm in diameter in an Ar-filled glovebox. Subsequently, mechanical alloying was performed on a high energy ball mill (SPEX 8000D) for 6 h, with the powders being loosed every 2 h. The obtained powders were then compacted using a field-assisted sintering technique (FAST, FCT Systeme GmbH) at 1373 K and 50 MPa for 3 min in a vacuum. The sintered samples were cut and polished to the desired sizes for measuring the thermoelectric properties.

Transport Property Measurement: Electrical transport properties, including electrical conductivity (σ), and Seebeck coefficient (α) were measured using a commercial device (LSR-3, Linseis). High-temperature thermal conductivities were calculated by $\kappa = \lambda \rho C_p$, where λ is the thermal diffusivity, ρ is the density and C_p is the specific heat. λ was measured by a laser flash system (LFA1000, Linseis). C_p is estimated from the Dulong-Petit law, ρ was determined by the Archimedes method. Hall concentrations (n_H) were measured by a physical property measurement system (Versalab, Quantum Design) at room temperature using the Hall bar method with ±3 T magnetic induction. The Hall mobility (μ_H) is calculated by $\mu_H = \sigma / n_H e$, where e is the unit charge. The measurement errors are 4%, 5%, and 6% for electrical resistivity, Seebeck coefficient, and thermal conductivity, respectively. Explicitly, the uncertainties of thermal conductivity originate from 2% in mass density, 4% in diffusivity. Therefore,
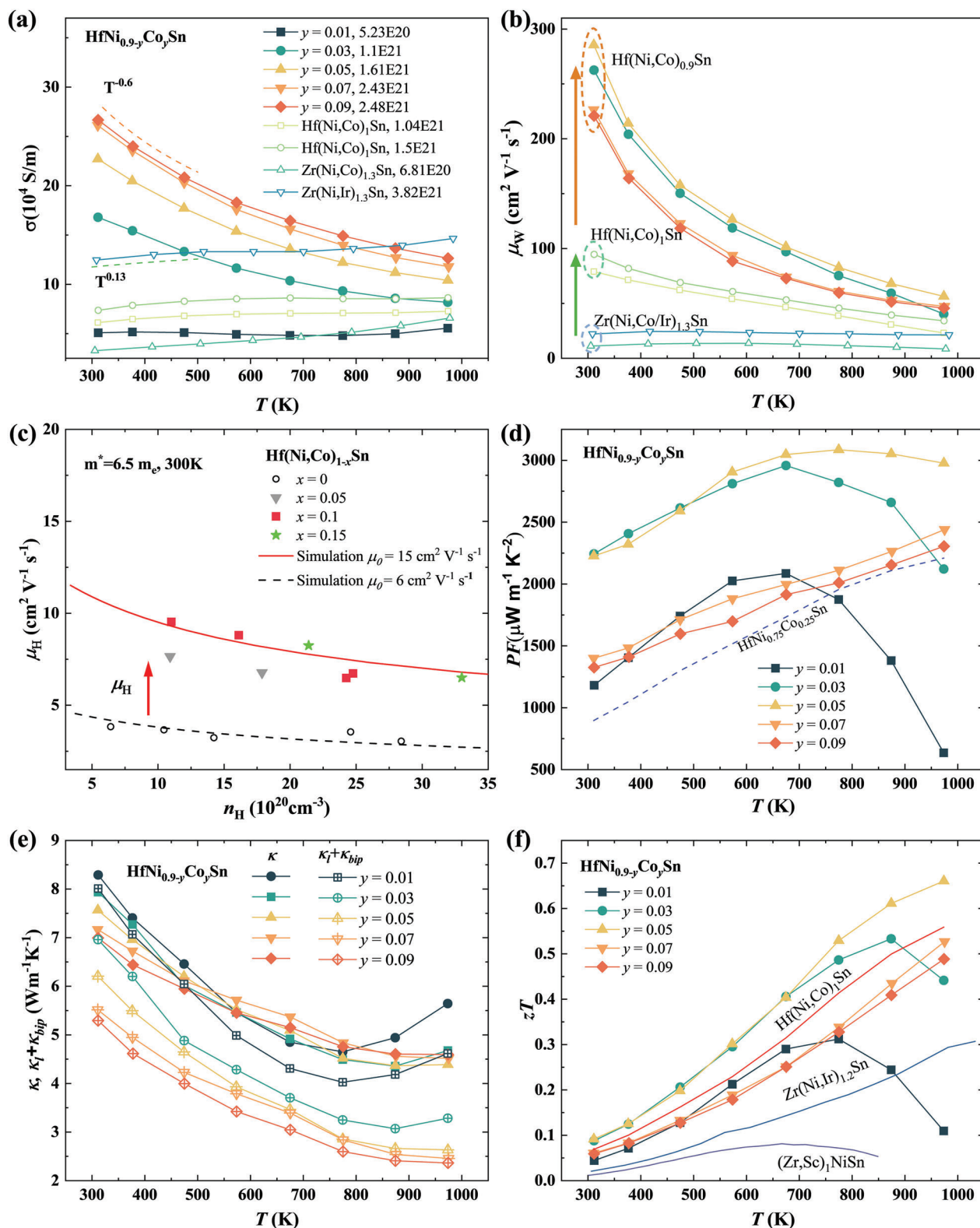
**ADVANCED
SCIENCE NEWS**

www.advancedsciencenews.com

**ADVANCED
ENERGY
MATERIALS**

www.advenergymat.de

Figure 5. Improvement of thermoelectric properties. a) Temperature-dependent electrical conductivity and b) weighted mobility of HfNi$_{0.9-y}$Co$_y$Sn in comparison with previously reported data.[35,41] c) Hall mobility dependence on Hall carrier concentration of Hf(Ni, Co)$_{1-x}$Sn samples (x = 0, 0.05, 0.1, and 0.15) at 300 K, the data of x = 0 from the literature.[35] d) Temperature-dependent power factor. e) Temperature-dependent total thermal conductivity (κ) and lattice and bipolar thermal conductivity ($\kappa_l + \kappa_{bip}$). f) Temperature-dependent zT in comparison with reported data.[32,35,41]

according to error propagation, the uncertainties in power factor and zT are 10% and 15%, respectively.

Microstructure Characterization: Bulk XRD of all samples was performed on polished surfaces using a Bruker D8 Advance diffractometer with a Co Kα source to characterize the phases. The high-resolution X-ray powder diffraction patterns were collected on a STOE Stadi P diffractometer with a Mo source, a Ge (111) monochromator and Mythen 1K detector (Dectris) that yields a single wavelength of 0.7093 Å in a flat sample transmission geometry. Rietveld analyses of the XRD patterns were performed using the FullProf software.[50] The microstructure was confirmed by field-emission SEM (Zeiss Sigma 300) and energy-dispersive X-ray spectroscopy (EDX) was applied to study the elemental distribution. TEM and high-angle annular dark field (HAADF)-STEM investigations were carried out by using a JEM-ARM 200F electron microscope equipped with a cold FEG source and double-Cs correctors operated at 200 kV. The samples ground to powder were characterized by ICP-OES (iCAP 6500 Duo View, Thermo Fisher Scientific) for elemental ratios with a standard deviation of $\approx$1% for each element.

Theoretical Calculations: The density functional theory (DFT) calculations were conducted by the plane-wave pseudopotential method using the Vienna ab initio simulation package (VASP). A supercell cell consisting of 8 ($2 \times 2 \times 2$) units was adopted for structural relaxation and electron band calculations. The projector augmented wave (PAW) method pseudopotentials with the Perdew–Burke–Ernzerhof generalized gradient approximation (GGA-PBE) functional were used to describe the electron-ion interactions.[51–53] A $3 \times 3 \times 3$ k-mesh grid generated by the Monkhorst-Pack scheme (Gamma-centered) was used to sample the Brillouin zone. The electron wave functions expand into a basis set of plane waves with a kinetic-energy cutoff of 450 eV. All lattice parameters and atomic positions are relaxed. The total energy convergence was set to be $<1 \times 10^{-5}$ eV and the force convergence was set to be <0.03 V Å^{-1} on the atoms. A band-unfolding technique was applied to get the band structure of defective HfNiSn from supercell calculations.[54]

Supporting Information

Supporting Information is available from the Wiley Online Library or from the author.

Conflict of Interest

The authors declare no conflict of interest.

Data Availability Statement

The data that support the findings of this study are available from the corresponding author upon reasonable request.

[1] L. E. Bell, *Science* **2008**, *321*, 1457.
[2] G. J. Snyder, E. S. Toberer, *Nat. Mater.* **2008**, *7*, 105.
[3] Q. Zhang, K. Deng, L. Wilkens, H. Reith, K. Nielsch, *Nat. Electron.* **2022**, *5*, 333.
[4] T. Zhu, Y. Liu, C. Fu, J. P. Heremans, J. G. Snyder, X. Zhao, *Adv. Mater.* **2017**, *29*, 1605884.
[5] T.-R. Wei, M. Guan, J. Yu, T. Zhu, L. Chen, X. Shi, *Joule* **2018**, *2*, 2183.
[6] J. Zhang, D. Ishikawa, M. M. Koza, E. Nishibori, L. Song, A. Q. R. Baron, B. B. Iversen, *Angew. Chem., Int. Ed.* **2023**, *135*, 202218458.
[7] J. Mao, Z. Liu, J. Zhou, H. Zhu, Q. Zhang, G. Chen, Z. Ren, *Adv. Phys.* **2018**, *67*, 69.
[8] R. He, G. Schierning, K. Nielsch, *Adv. Mater. Technol.* **2018**, *3*, 1700256.
[9] Z. Liu, S. Guo, Y. Wu, J. Mao, Q. Zhu, H. Zhu, Y. Pei, J. Sui, Y. Zhang, Z. Ren, *Adv. Funct. Mater.* **2019**, *29*, 1905044.
[10] Y. Pei, X. Shi, A. LaLonde, H. Wang, L. Chen, G. J. Snyder, *Nature* **2011**, *473*, 66.
[11] Y. Tang, Z. M. Gibbs, L. A. Agapito, G. Li, H.-S. Kim, M. B. Nardelli, S. Curtarolo, G. J. Snyder, *Nat. Mater.* **2015**, *14*, 1223.
[12] F. Jia, X. Yin, W.-W. Cheng, J.-T. Lan, S.-H. Zhan, L. Chen, L.-M. Wu, *Angew. Chem., Int. Ed.* **2023**, *135*, 202218019.
[13] X. Su, P. Wei, H. Li, W. Liu, Y. Yan, P. Li, C. Su, C. Xie, W. Zhao, P. Zhai, Q. Zhang, X. Tang, C. Uher, *Adv. Mater.* **2017**, *29*, 1602013.
[14] X. Xu, Y. Huang, X. Liu, B. Jia, J. Cui, R. He, J. Wang, Y. Luo, K. Nielsch, J. He, *Energy Environ. Sci.* **2022**, *15*, 4058.
[15] N. A. Heinz, T. Ikeda, Y. Pei, G. J. Snyder, *Adv. Funct. Mater.* **2014**, *24*, 2135.
[16] S. Chanakian, W. Peng, V. Meschke, A. K. M. Ashiquzzaman Shawon, J. Adamczyk, V. Petkov, E. Toberer, A. Zevalkink, *Angew. Chem., Int. Ed.* **2023**, *62*, 202301176.
[17] B. Jiang, Y. Yu, J. Cui, X. Liu, L. Xie, J. Liao, Q. Zhang, Y. Huang, S. Ning, B. Jia, B. Zhu, S. Bai, L. Chen, S. J. Pennycook, J. He, *Science* **2021**, *371*, 589.
[18] S. Shafeie, S. Guo, Q. Hu, H. Fahlquist, P. Erhart, A. Palmqvist, *J. Appl. Phys.* **2015**, *118*, 184905.
[19] X. Li, K. Lu, *Science* **2019**, *364*, 733.
[20] Y. Qin, B. Qin, T. Hong, X. Zhang, D. Wang, D. Liu, Z.-Y. Wang, L. Su, S. Wang, X. Gao, Z.-H. Ge, L.-D. Zhao, *Science* **2024**, *383*, 1204.
[21] D. Liu, D. Wang, T. Hong, Z. Wang, Y. Wang, Y. Qin, L. Su, T. Yang, X. Gao, Z. Ge, B. Qin, L.-D. Zhao, *Science* **2023**, *380*, 841.
[22] M. Zhang, Z. Gao, Q. Lou, Q. Zhu, J. Wang, Z. Han, C. Fu, T. Zhu, *Adv. Funct. Mater.* **2024**, *34*, 2307864.
[23] J. Dong, F.-H. Sun, H. Tang, J. Pei, H.-L. Zhuang, H.-H. Hu, B.-P. Zhang, Y. Pan, J.-F. Li, *Energy Environ. Sci.* **2019**, *12*, 1396.
[24] T. Graf, C. Felser, S. S. P. Parkin, *Prog. Solid State Chem.* **2011**, *39*, 1.
[25] S. Chen, Z. Ren, *Mater. Today* **2013**, *16*, 387.
[26] Y. Liu, C. Fu, K. Xia, J. Yu, X. Zhao, H. Pan, C. Felser, T. Zhu, *Adv. Mater.* **2018**, *30*, 1800881.
[27] H. Xie, H. Wang, Y. Pei, C. Fu, X. Liu, G. J. Snyder, X. Zhao, T. Zhu, *Adv. Funct. Mater.* **2013**, *23*, 5123.
[28] K. S. Kim, Y.-M. Kim, H. Mun, J. Kim, J. Park, A. Y. Borisevich, K. H. Lee, S. W. Kim, *Adv. Mater.* **2017**, *29*, 1702091.
[29] G. Rogl, K. Yubuta, V. V. Romaka, H. Michor, E. Schafler, A. Grytsiv, E. Bauer, P. Rogl, *Acta Mater.* **2019**, *166*, 466.
[30] A. N. Gandi, U. Schwingenschlögl, *Phys. Chem. Chem. Phys.* **2016**, *18*, 14017.
[31] W. G. Zeier, J. Schmitt, G. Hautier, U. Aydemir, Z. M. Gibbs, C. Felser, G. J. Snyder, *Nat. Rev. Mater.* **2016**, *1*, 16032.

[32] J. Schmitt, Z. M. Gibbs, G. J. Snyder, C. Felser, *Mater. Horiz.* **2015**, *2*, 68.

[33] Y. G. Yu, X. Zhang, A. Zunger, *Phys. Rev. B* **2017**, *95*, 085201.

[34] K. Tolborg, B. B. Iversen, *Chem. Mater.* **2021**, *33*, 5308.

[35] X. Ai, B. Lei, M. O. Cichocka, L. Giebeler, R. B. Villoro, S. Zhang, C. Scheu, N. Pérez, Q. Zhang, A. Sotnikov, D. J. Singh, K. Nielsch, R. He, *Adv. Funct. Mater.* **2023**, *33*, 2305582.

[36] F. Aliev, A. Belogorokhov, N. Brandt, V. Kozyr'kov, R. Skolozdra, Y. Stadnyk, *ZhETF Pisma Redaktsiiu* **1988**, *47*, 184.

[37] C. Fu, M. Yao, X. Chen, L. Z. Maulana, X. Li, J. Yang, K. Imasato, F. Zhu, G. Li, G. Auffermann, U. Burkhardt, W. Schnelle, J. Zhou, T. Zhu, X. Zhao, M. Shi, M. Dressel, A. V. Pronin, G. J. Snyder, C. Felser, *Adv. Sci.* **2020**, *7*, 1902409.

[38] H. J. Goldsmid, J. W. Sharp, *J. Electron. Mater.* **1999**, *28*, 869.

[39] F. G. Aliev, V. V. Kozyrkov, V. V. Moshchalkov, R. V. Scolozdra, K. Durczewski, *Z. Physik B – Condensed Matter* **1990**, *80*, 353.

[40] H.-H. Xie, C. Yu, B. He, T.-J. Zhu, X.-B. Zhao, *J. Electron. Mater.* **2012**, *41*, 1826.

[41] Y. Kimura, T. Tanoguchi, T. Kita, *Acta Mater.* **2010**, *58*, 4354.

[42] R. V. Skolozdra, Y. V. Stadnik, E. Eh. Starodynova, *Ukrainskij Fizicheskij Zhurnal* **1986**, *31*, 1258.

[43] H. M. Rietveld, *J. Appl. Crystallogr.* **1969**, *2*, 65.

[44] Y. Matfaing, *Prog. Cryst. Growth Charact.* **1981**, *4*, 317.

[45] Z. Li, W. Xue, S. Han, Z. Gao, A. Li, X. Zhao, Y. Wang, C. Fu, T. Zhu, *Mater. Today Phys.* **2023**, *34*, 101072.

[46] R. He, T. Zhu, Y. Wang, U. Wolff, J.-C. Jaud, A. Sotnikov, P. Potapov, D. Wolf, P. Ying, M. Wood, Z. Liu, L. Feng, N. Pérez Rodríguez, G. J. Snyder, J. C. Grossman, K. Nielsch, G. Schierning, *Energy Environ. Sci.* **2020**, *13*, 5165.

[47] X. Li, H. Yao, S. Duan, X. Bao, W. Xue, Y. Wang, F. Cao, M. Li, Z. Chen, Y. Wang, X. Lin, X. Liu, Z. Feng, J. Mao, Q. Zhang, *Acta Mater.* **2023**, *244*, 118591.

[48] Z. Li, C. Zhao, C. Xiao, *Chem. – Asian J.* **2020**, *15*, 4124.

[49] M. K. Brod, S. Anand, G. J. Snyder, *Adv. Electron. Mater.* **2022**, *8*, 2101367.

[50] T. Roisnel, J. Rodríquez-Carvajal, *MSF* **2001**, *118*, 378.

[51] G. Kresse, D. Joubert, *Phys. Rev. B* **1999**, *59*, 1758.

[52] G. Kresse, J. Furthmüller, *Phys. Rev. B* **1996**, *54*, 11169.

[53] J. P. Perdew, K. Burke, M. Ernzerhof, *Phys. Rev. Lett.* **1996**, *77*, 3865.

[54] V. Wang, N. Xu, J.-C. Liu, G. Tang, W.-T. Geng, *Comput. Phys. Commun.* **2021**, *267*, 108033.